THE JOURNAL OF PHYSICAL CHEMISTRY C

pubs.acs.org/JPCC Article

Oxygen Vacancy-Related Cathodoluminescence Quenching and Polarons in CeO_2

Thanveer Thajudheen, Alex G. Dixon, Sandra Gardonio, Iztok Arčon, and Matjaz Valant*

Cite This: J. Phys. Chem. C 2020, 124, 19929–19936

Read Online

ACCESS | Metrics & More | Article Recommendations

ABSTRACT: We used cathodoluminescence (CL) spectroscopy to characterize the oxygen vacancies (V_O) in ceria (CeO_2). The effects of the processing atmosphere and thermal quenching temperature on the nature and distribution of the intrinsic defects and on the spectroscopic behavior were investigated. The presence of polarons and associates of the polarons with the oxygen vacancies such as $(V_O^{\bullet\bullet}-Ce'_{Ce})^{\bullet}$ is demonstrated. CL intensity quenching above a critical concentration of V_O has been shown. Even though the emission centers in all samples are the same, their concentration changes with the oxygen partial pressure of the processing atmosphere. Deconvolution of the observed CL spectra shows that the emissions originating from the F^0 centers prevail over those of F^+ centers of V_O when the defect concentration is high.

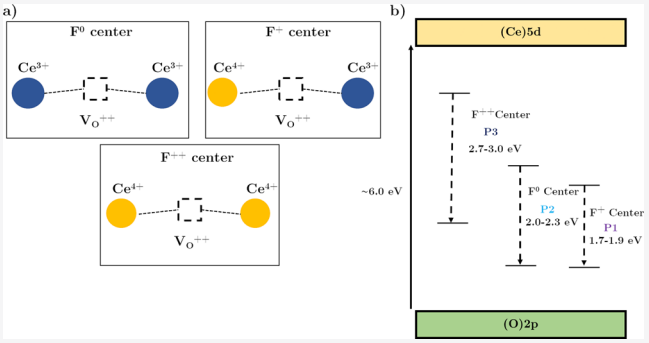

INTRODUCTION

Because of its fundamental ability to accommodate a large number of defects without destabilizing the crystal structure, cerium oxide (ceria, CeO_2) has become a technologically important material that finds its use in many areas. Perhaps, the most widespread of which is its application in automobile exhausts as a catalyst[1] because of its ability to absorb and release oxygen under oxidizing and reducing conditions. From a crystallographic point of view, this means that the ceria crystal structure can tolerate a high density of oxygen vacancies and reduced cerium ions, Ce^{3+}. The density of these defects is associated with the external oxygen partial pressure.

Other important properties of CeO_2, such as a high dielectric constant and good epitaxy on the Si substrate, make it a potential material for future microelectronic applications. In particular, epitaxial CeO_2 films are considered to be very promising candidates for high quality and highly stable insulating thin films.[2] There have been extensive studies on defects in ceria, which focused on their formation by doping, treatment in reductive or oxidative atmosphere,[3,4] and the dependence on a crystal size[5,6] and atomic surface structures.[7,8]

Despite its ability to unravel the defect structures of crystals, cathodoluminescence (CL) spectroscopy has found little use in the study of CeO_2 emissions related to oxygen vacancies. CL spectroscopy is highly sensitive to relatively low defect concentrations and can be used to determine carrier recombination pathways that involve these defects. This makes it a technique of choice for studies of the defect structures in bulk and nanostructures.[9] Previously, it has been shown that CL can be used as a direct tool for studying the oxygen vacancy concentration in the vicinity of oxide surfaces.[10] CL is also able to provide information on mechanical stresses originating from oxygen vacancies.[11]

The emissions associated with oxygen vacancies in ZrO_2-related materials, as well as Al_2O_3 and TiO_2, have been studied by spectrally and spatially resolved CL spectroscopy.[12,13] It has been reported that the CL intensity for Y-doped ZrO_2 decreases with an increase in the concentration of oxygen vacancies. In this study, Boffelli et al.[11] proposed two hypotheses to explain the observed intensity quenching. The first hypothesis, called the "strained lattice hypothesis", states that because the efficiency of the CL intensity is directly related to Zr−O bond stretching and the increased concentration of oxygen vacancies redistributes the highly localized lattice strain, the CL emission intensity lowers with the higher vacancy concentration. The second, the "charge trap hypothesis", states that the decrease in the CL intensity under the electron excitation occurs because of the fact that the oxygen vacancies act as charge traps and thereby decrease the

Received: May 22, 2020
Revised: July 24, 2020
Published: August 18, 2020

https://dx.doi.org/10.1021/acs.jpcc.0c04631
J. Phys. Chem. C 2020, 124, 19929−19936

number of available electrons; the more the vacancy sites, the lower the CL intensity.

The presence of charged vacancies is put forth to explain many of the experimental observations. The possibility of the formation of oxygen vacancy complexes has been proposed and experimentally observed. In the case of doped ceria, a conductivity maximum has been observed as a function of dopant concentration.[14] Initially, it was explained by the presence of a minimum in the activation enthalpy as the dopant concentration increases. Later, this was rejected by Faber et al.[15] who argued that the lattice relaxations around the dopant ions will screen any columbic effects arising from the dopant. They ascribe the presence of the minimum to changes in the energy of the oxygen sites in the vicinity of the dopant. Altogether, it is proposed that the presence of this minimum in the concentration dependence of the activation enthalpy can be taken as an indicator of defect association, which limits the conductivity of doped ceria.[16]

The objective of this work is to demonstrate the CL behavior of CeO_2 and its dependence on oxygen vacancy concentration. We report that the intrinsic oxygen vacancies in CeO_2 cause CL intensity quenching when only above a critical concentration. It is shown that a careful understanding of CL emissions of CeO_2 could help to comprehend the interaction between vacancy centers. We examine the possibility of oxygen vacancy association with electron polarons and their consequence on the occurrence of differing charge states of the intrinsic point defects in CeO_2. The ability of the CL technique to explore different charge states of intrinsic point defects is demonstrated.

METHODS

High-purity CeO_2 nanopowders (Sigma-Aldrich, 99.95% pure, size <50 nm) were sintered at 1450 °C for 8 h in air (C-A), oxygen (C-O), and nitrogen (C-N). In the second step, all the three samples were subjected to quenching after 10 h of annealing at different temperatures to achieve a frozen state with differing defect concentrations. The systematic change in defect concentration was verified by electrical impedance analysis.

A Rigaku MiniFlex diffractometer was used for the XRD measurements. Ni-filtered Cu Kα radiation, steps of 0.05° with a collection time of 1 s per step, was used to acquire the data. XRD was analyzed using X'Pert HighScore software.

Microstructural images and CL spectra were taken using a field-emission gun scanning electron microscope [SEM JEOLJSM 7100 TTLS (FEG)]. For the CL measurements, the same experimental conditions were applied for all samples to avoid introducing additional variables. The acceleration voltage and the beam current were set for all experiments at 25 keV and 2 nA, respectively. The CL spectra were acquired in the wavelength region 300−800 nm. The reported CL spectra have been corrected by grating response and detector response in the wavelength region 350−750 nm. The microscope was equipped with a CL device (GATAN MonoCL4) consisting of a parabolic mirror and a bundle of optical fibers used to collect and to focus the electron-stimulated luminescence emitted by the sample into a monochromator with 2 nm spectral resolution.

The dielectric properties of the samples (pellets) were studied using a frequency response analyzer (Agilent LCR E4980A). The impedance curves were obtained over a frequency range from 100 Hz to 2 MHz, using a two-probe measurement with copper tape electrodes in a capacitor geometry.

X-ray absorption spectra in the energy range of Ce L_3 edge (5724 eV) of the high-purity CeO_2 nanopowder samples, before sintering and sintered at 1450 °C for 8 h in air (C-A), oxygen (C-O), and nitrogen (C-N), and crystalline $CeVO_4$ as a reference for Ce^{3+} were measured in the transmission detection mode at the XAFS beamline of the ELETTRA synchrotron radiation facility in Trieste, Italy. A Si(111) double-crystal monochromator was used with an energy resolution of about 0.6 eV at 6 keV. Higher harmonics were eliminated by detuning of the second monochromator crystal to 60% of the maximum in the rocking curve. The intensity of the monochromatic X-ray beam was measured using three 30 cm-long consecutive ionization detectors filled with optimal gas mixtures for a given energy range: 350 mbar N_2 and 1650 mbar He (first); 1900 mbar N_2 and 100 mbar He (second); and 230 mbar Ar, 1000 mbar N_2, and 670 mbar He (third).

The CeO_2 samples were prepared in the form of homogeneous pellets, pressed from micronized powder mixed with micronized boron nitride (BN), with a total absorption thickness of about 1 above the Ce L_3 edge, and placed in the monochromatic beam between the first two ionization detectors. The absorption spectra were measured in the energy region from −150 to +400 eV relative to the Ce L_3 edge. Scans were stopped at the Ce L_2 edge (6165 eV). Equidistant energy steps of 0.3 eV were used in the X-ray absorption near-edge spectroscopy (XANES) region, while for the extended X-ray absorption fine structure region, equidistant k steps of 0.03 $Å^{-1}$ were adopted, with an integration time of 2 s/step. The exact energy calibration was established with simultaneous absorption measurement on the nanopowder CeO_2 reference sample placed between the second and the third ionization chambers. Absolute energy reproducibility of the measured spectra was ±0.03 eV. The quantitative analysis of XANES spectra was performed with the Demeter (IFEFFIT) program package.[17]

RESULTS AND DISCUSSION

Samples C-O, C-A, and C-N have been sintered in oxygen, air, and nitrogen atmospheres, respectively, with the scope of obtaining CeO_2 samples having an increasing concentration of oxygen vacancies because of processing in higher to lower oxygen partial pressure atmospheres.

Scanning electron microscopy showed no detectable difference in the microstructures of the investigated samples. The level of porosity and grain size are the same for all the samples. XRD analysis showed the presence of the pure CeO_2 phase with no traces of Ce_2O_3. A typical microstructure and XRD are shown in Figure 1.

The relative amounts of Ce^{4+} and Ce^{3+} species in the catalyst after sintering in different atmospheres were determined from the Ce L_3-edge XANES spectra. Different local environments of the Ce cation result in different L3-edge profiles in the XANES spectra, and the energy position of the absorption edge is correlated with the valence state of the absorbing atom in the sample. With increasing oxidation state, the absorption edge is shifted to higher energies. In the case of Ce^{3+} cations, a characteristic peak is present at 5726 eV, while Ce^{4+} cations can be identified by two characteristic peaks, at 5730 and 5736 eV.[18−20] A detailed comparison of the three XANES spectra show that the spectra of C-O and C-A samples are identical within the noise level, while the spectrum of the C-N sample

https://dx.doi.org/10.1021/acs.jpcc.0c04631
J. Phys. Chem. C 2020, 124, 19929−19936

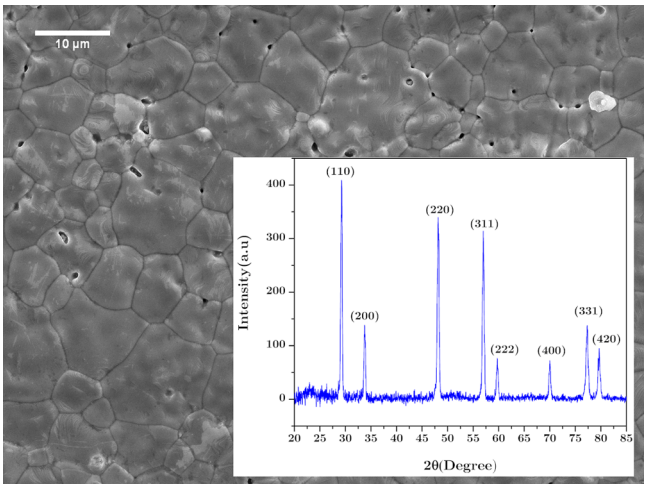

Figure 1. SEM micrograph and XRD (inset) acquired from the C-N sample. All sample preparations showed a similar structure with no variation in porosity or grain size.

sintered in nitrogen exhibits some differences in the pre-edge region at 5726 eV, which can be ascribed to the presence of a small amount of Ce^{3+} in the crystal structure of CeO_2. Relative amounts of Ce^{3+} species are quantitatively determined by a linear combination fit analysis.[17,20] The XANES spectrum of the CeO_2 sintered in nitrogen (C-N) can be completely described by a linear combination of three reference XANES profiles (Figure 2): the spectrum of CeO_2 nanopowder

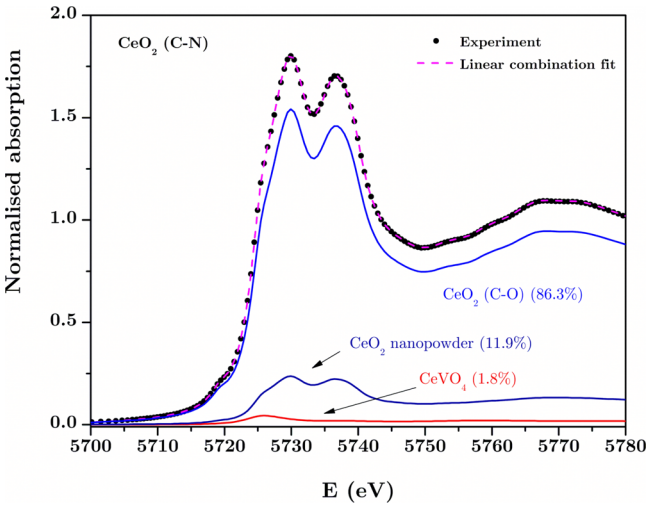

Figure 2. Ce L3-edge XANES spectrum of the CeO_2 nanopowder sample sintered in nitrogen (C-N). Dots are experimental data; the dashed magenta line is the best fit from a linear combination of reference Ce L3-edge XANES profiles [86.3% CeO_2 nanopowder sintered in oxygen (C-O) as a reference for Ce^{4+} (blue), 11.9% crystalline unsintered CeO_2 nanopowder as a reference for Ce^{4+} (dark blue), and 1.8% crystalline $CeVO_4$ as a reference for Ce^{3+} (red)].

sintered in oxygen (C-O) (86.3%), the spectrum of crystalline unsintered CeO_2 nanopowder (11.9%) as references for Ce^{4+}, and the spectrum of $CeVO_4$ as reference for Ce^{3+} (1.8%). Statistical uncertainty for the relative amount of Ce^{3+} is ±0.1%. Evidentially, the presence of Ce^{3+} cations in the C-O and C-A samples, sintered in oxygen and in air, respectively, are below the detection limit of the method (<0.2%).

Figure 3a shows the representative CL spectra acquired under identical conditions on CeO_2 samples, sintered in different atmospheres. CL spectra of the different samples showed a pronounced variation in their intensities. All the three spectra are composed of a broad band, centered at approximately 550 nm (2.25 eV), along with two additional narrow peaks at 575 nm (2.15 eV) and 617 nm (2.00 eV).

The narrow peaks in the spectra were recognized as emissions from impurities. It is known from photoluminescence (PL) studies that Sm^{3+} gives emissions corresponding to the transitions $^4G_{5/2}$ to $^6H_{5/2}$ and $^4G_{5/2}$ to $^6H_{7/2}$ within the range 550 nm (2.25 eV) to 800 nm (1.54 eV).[21] The presence of 0.4 mg/kg Sm impurity has been confirmed in our starting CeO_2 powder by inductively coupled plasma mass spectrometry. Correspondingly, the narrow emission lines are assigned to the Sm impurity similarly to in Balestrieri et al.[21] The Sm^{3+} concentration is constant throughout all the samples because all samples used the same starting CeO_2 powder.

Calculations[22] predict that for CeO_2 with a neutral oxygen vacancy ($V_O^\times$ according to Kroger−Vink notation), the electronic density of states has two gap states between the O 2p and the Ce 4f bands, lying well inside the band gap. Because the two band gaps of CeO_2 are beyond the observed emission lines, it is reasonable to conclude that the emission centered at 550 nm originates from the defect energy levels within the band gap which can act like electron traps. The oxygen vacancies, $V_O^\times$, and their surrounding Ce ionic species can be described as Farbe centers or F centers, as discussed later on and detailed in Figure 6a, with F^{++} indicating a vacancy surrounded by Ce^{4+} ions, F^+ indicating a single Ce^{3+} adjacent to an oxygen vacancy, and F^0 indicating a vacancy with two peripheral Ce^{3+} ions (note that charge neutrality is not shown). It has been shown[22] that the gap states of $V_O^\times$ lay at 1.75 eV, whereas the gap state of $V_O^\bullet$ lies near the mid gap at about 2.25 eV. Several PL studies on CeO_2 reported bands in the region 2.07−2.35 eV and ascribed these to electron transitions from the excited state (F^0*) of the neutral oxygen vacancies to the corresponding ground state (F^0).[23,24] The other defect types that give rise to energy states within the band gap are cerium vacancy (V_{Ce}) at 2.75 eV, interstitial cerium (I_{Ce}) at 1.85 eV, and Frenkel defect at 1.02 eV. Because the formation energies for these defects are very high compared to V_O, they should not contribute to the CL emission because of their low concentration.[22]

A discernible variation in the CL intensity (see Figure 3a) revealed the influence of defect concentration on the emissions of CeO_2. Conventional wisdom suggests that we should observe a linear relationship between the CL intensity and concentration of defects, that is, the emission intensity should increase with the defect concentration.[11,25−27] Surprisingly, the intensity of the C-O sample lies in between the C-N and C-A samples. Accordingly, we deduce that as the concentration of V_O increases, the CL intensity increases up to some critical concentration, where it then reaches a maximum and decreases.

Figure 4 shows the room temperature frequency dependence of the dielectric constant (ε') and dielectric loss (ε'') measured from 100 Hz to 2 MHz. The values of ε' and ε'' are extracted from impedance analysis. The existence of a polaron state can be seen mainly from the dielectric loss (ε'') at high frequencies because of hopping conduction with a classical power-law dependence versus frequency. The dielectric constant increases significantly with increasing oxygen vacancies from C-O to C-

https://dx.doi.org/10.1021/acs.jpcc.0c04631
J. Phys. Chem. C 2020, 124, 19929−19936

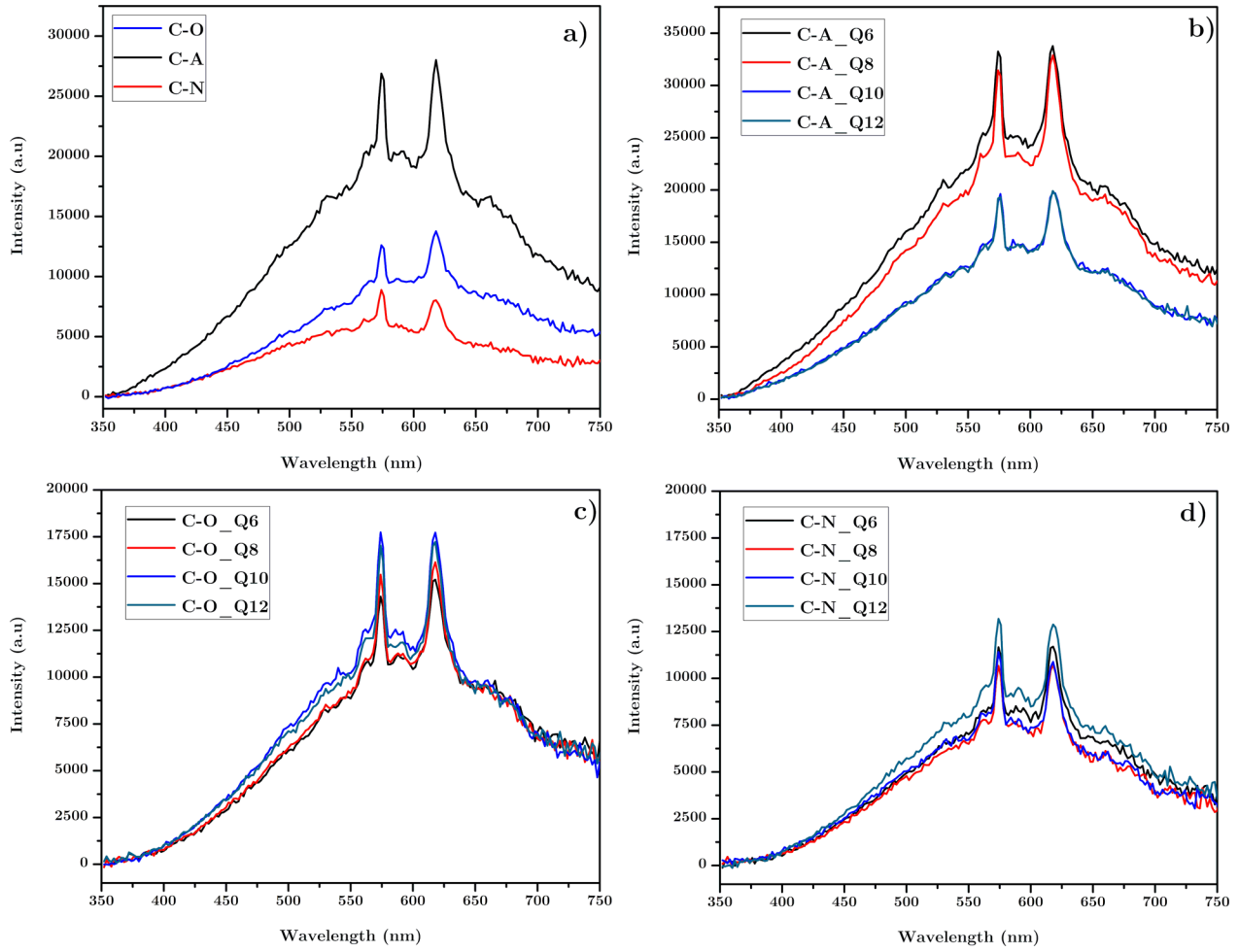

Figure 3. (a) CL spectra collected for CeO_2 samples sintered in air (C-A), oxygen (C-O), and nitrogen (C-N) atmospheres. CL spectra for samples thermally quenched from different temperatures in (b) air, (c) oxygen, and (d) nitrogen atmospheres. Q6, Q8, Q10, and Q12 stand for thermal quenching at 600 °C, 800 °C, 1000 °C, and 1200 °C, respectively. The C-A samples show a higher overall CL intensity and higher temperature dependence in vacancy formation.

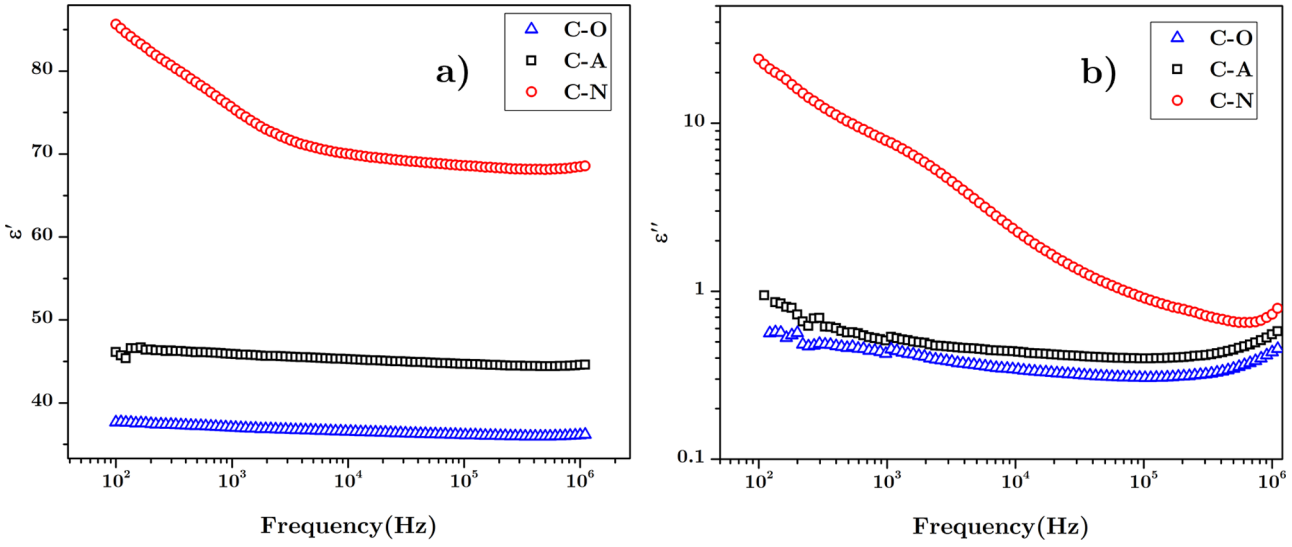

Figure 4. Room temperature frequency dependence of the (a) real part of the dielectric constant ε' and (b) imaginary part of the dielectric constant ε'' for CeO_2 samples sintered in air, oxygen, and nitrogen atmospheres, showing an increase in dielectric constant with decreasing oxygen partial pressure of the processing atmosphere.

https://dx.doi.org/10.1021/acs.jpcc.0c04631
J. Phys. Chem. C 2020, 124, 19929−19936

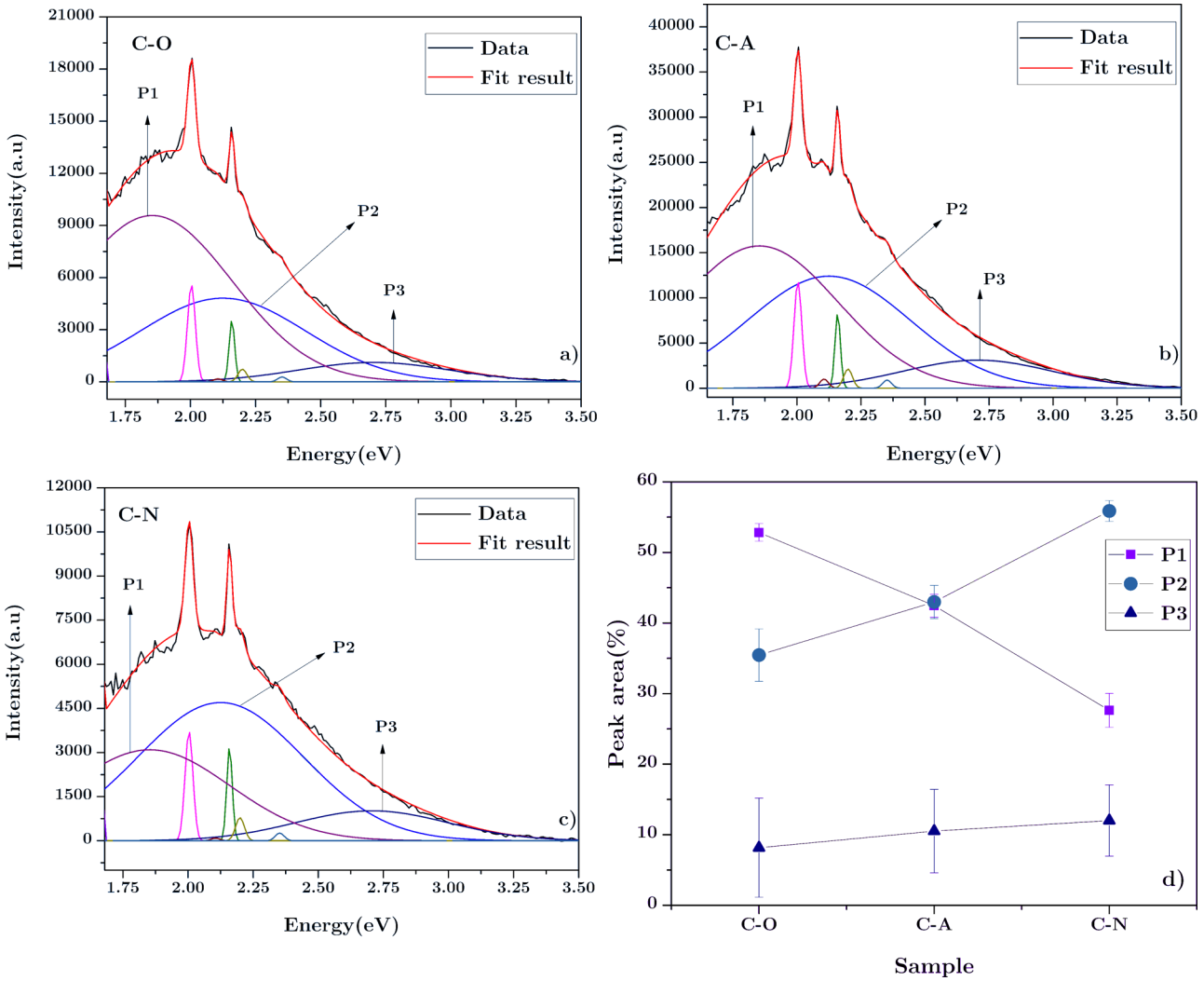

Figure 5. (a–c). Gaussian deconvolution of the CL spectra collected from the CeO_2 samples sintered in oxygen, air, and nitrogen, respectively; (d) peak area percentage, that is, the ratio of P1 (purple), P2 (blue), P3 (dark blue) peak areas to their overall sum for each of the CL spectra.

N. The greater polarizability of a crystal with structural point defects as compared to an ideal defect-free crystal can be explained mainly by the high polarizability of the two electrons trapped in the vacant sites and the reduction in bond stiffness. According to the literature,[28] V_O reduces the bond stiffness of some bonds which increases bond deformation. Because the bonds with reduced stiffness in the defective oxides deform more readily under an electric field, this also means that they are more readily polarized. This substantiates that the V_O concentration increases in the order C-O < C-A < C-N. Moreover, from the XANES analysis, we have seen that for the C-O and C-A samples, the presence of Ce^{3+} cations was below the detection limit for the method, whereas in the C-N sample, the amount of Ce^{3+} ions was estimated at 1.8%.

To further investigate the dependence of the defect concentration on the CL intensity, we performed a series of experiments where we thermally quenched the samples at different temperatures and in different atmospheres, the results of which are depicted in Figure 3b–d. For the C-A sample, it was found that the CL intensity decreases with the increase in quenching temperature (Figure 3b), while for C-O (Figure 3c) and C-N (Figure 3d), the intensity stays nearly constant. The observed variations in the CL intensity can be explained by the fact that processing CeO_2 in different atmospheres sets different initial oxygen vacancy concentrations, which are later varied as a function of quenching temperature. In the C-O samples, the oxidation potential of the oxygen atmosphere limits the creation of oxygen vacancies, and this effect strongly dominates over any thermal variation; thus, quenching temperature has little effect on the vacancy concentration. However, in the C-A samples, the oxygen partial pressure is significantly lower and the thermal quenching temperature can lead to a considerable variation of the defect concentration and thus the CL intensity. In contrast, the quenched C-N samples all show very similar emission intensities because of similar vacancy concentrations. This can be explained with the fact that for high vacancy concentration, the formation energy of new vacancies within the bulk progressively increases.[29,30] Therefore, there are no significantly more vacancies created at the higher temperatures and no significant variation in the CL intensity is seen.

A detailed understanding of the relative concentration of the different charge states of F centers associated to oxygen vacancies for the different CeO_2 samples has been obtained by curve fitting analysis of CL spectra, as reported in Figure 3a. For the deconvolution of the spectral lines, a set of eight

https://dx.doi.org/10.1021/acs.jpcc.0c04631
J. Phys. Chem. C 2020, 124, 19929–19936

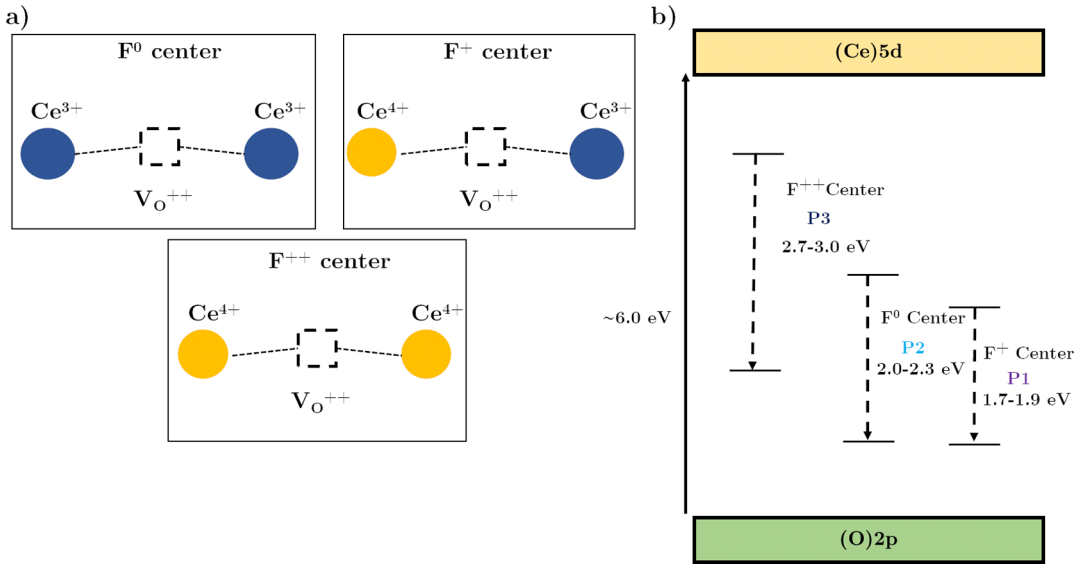

Figure 6. (a) Schematic illustration of the different electronic configurations of oxygen vacancies in CeO_2 and their respective F centers (note that charge neutrality is not shown).[35] (b) Illustration of the radiative electronic transitions in CeO_2 with their corresponding CL peaks and F centers.

Gaussian bands were used, and the results are reported in Figure 5. Note that the wavelength dispersion is presented in the energy scale (eV) so that a meaningful comparison of the spectral weights of the components becomes possible.

Five sharp peaks are found at 2.00, 2.10, 2.16, 2.20, and 2.35 eV, while three much broader peaks are located at 1.87, 2.11, and 2.70 eV referred to as P1, P2, and P3, respectively. The sharp peaks are the clear signature of the Sm trace impurity in the purchased CeO_2 powder, as discussed above.

From Figure 5d, it is clear that as the oxygen partial pressure decreases and thus the vacancy concentration increases, the component P2 grows at the expense of P1, whereas the P3 component stays relatively constant.

The band observed at 1.87 eV (P1) can result from the radiative emission of the transition from the F^+ state to the valence band.[23] This is supported by the fact that the electrons from the valence band cannot be excited to the F^0 ground state, whereas the $4f^1$ band is positioned at only 1.2−1.5 eV above the valence band.[31,32] According to the calculations,[22] $V_O^{\bullet}(F^+)$ should never be the most stable charge state, yet it shows a strong CL emission. One proposed mechanism for this discrepancy would be disproportionation, according to the reaction $2V_O^{\bullet} \rightarrow V_O^{\times} + V_O^{\bullet\bullet}$, leaving a neutral ($V_O^{\times}$) and a +2 charge state ($V_O^{\bullet\bullet}$). However, the experimental results do not support this mechanism because we have not observed any evidence of $V_O^{\bullet\bullet}$ expected at 3 eV.[23] Additionally, some studies[33,34] have dismissed this P1 peak as being a product of element impurity, but the clear trend we observe in this peak as a function of oxygen partial pressure indicates that this is unlikely to be the case. For this reason, we propose different mechanisms that are in full accordance with the experimental results presented and the calculations reported in the literature.[35−37]

It has been reported[38,39] that association between polarons and charged oxygen vacancies occurs to resemble neutral and singly charged oxygen vacancies as follows

$$V_O^{\bullet\bullet} + Ce'_{Ce} \rightarrow (V_O^{\bullet\bullet} - Ce'_{Ce})^{\bullet} \quad (1)$$

$$V_O^{\bullet\bullet} + 2Ce'_{Ce} \rightarrow (Ce'_{Ce} - V_O^{\bullet\bullet} - Ce'_{Ce})^{\times} \quad (2)$$

According to Zacherle et al.,[35] at high oxygen partial pressures, doubly charged oxygen vacancies $V_O^{\bullet\bullet}$ are the dominant vacancy species. Considering the energy of the formation of various charged defects, the next possible candidate is $(V_O^{\bullet\bullet}-Ce'_{Ce})^{\bullet}$ which resembles single-charged oxygen vacancy. Castleton et al.[40] showed that the energy level for $(V_O^{\bullet\bullet}-Ce'_{Ce})^{\bullet}$ is present at ∼1.7−2.0 eV. Because there is no distinction between $(V_O^{\bullet\bullet}-Ce'_{Ce})^{\bullet}$ and $V_O^{\bullet}$ except for the electronic structure of the two defect species, we ascribe emission P1 to Ce^{3+} in configuration of F^+ in Figure 6a.

Based on the calculations by Zacherle et al.[35] mentioned above, we attribute the CL band (P2) observed in the region 2.11 eV to F^0 center transition. At low oxygen partial pressures, the Ce^{3+} concentration increases and the cluster of a doubly charged oxygen vacancy with two polarons $(Ce'_{Ce}-V_O^{\bullet\bullet}-Ce'_{Ce})^{\times}$ becomes the energetically most favorable species; hence, P2 emission originates from the configuration equivalent to F^0.

From a crystallographic point of view, the reduction of CeO_2 introduces strain in the crystal lattice because of the formation of oxygen vacancies and Ce^{3+}, which has a larger ionic radius (1.01 Å and 0.87 Å for Ce^{3+} and Ce^{4+}, respectively).[41] The observed clustering of Ce^{3+} around the oxygen vacancies is driven by a reduction of the lattice strain and consequent reduction of free energy. With an increase in overall defect concentration, the strain increases, and the structure compensates by bringing yet another Ce^{3+} ion into the first coordination sphere around the vacancies. This explains why the increase in P2 emissions coincides with the decrease in P1 emissions.

The emission P3 in all the samples studied stays almost constant irrespective of processing atmosphere or temperature, with a slight increase as the oxygen partial pressure decreases. We ascribe this emission to F^{++} configuration which is consistent with Costantini et al.[34] According to them, the CL emission at P3 in CeO_2 originates from Ce^{3+} ions which are not spatially adjacent to oxygen vacancies. As the F^{++} configuration describes oxygen vacancies surrounded by Ce^{4+} ions, their presence would imply the vacancy electron localized on a Ce^{3+} ion at an undistorted site further from the vacancy.

https://dx.doi.org/10.1021/acs.jpcc.0c04631
J. Phys. Chem. C 2020, 124, 19929−19936

Therefore, we conclude that the observed trend in variation of bands can be explained as follows: at high oxygen partial pressure, Ce^{3+} ions are readily found in F^+ configuration, and the band P1 is the dominant emission in the C-O sample. As reduction induces more vacancies and thus more Ce^{3+} ions into the crystal structure, the configuration F^0 is favored; hence, P2 becomes dominant in the C-N samples. An illustration of the radiative electronic transitions on CeO_2 samples is reported in Figure 6b.

The increase in oxygen vacancy concentration will lead to a change in the crystal field around the vacancy centers, in turn, resulting in the energy levels that favor emission in the infrared region of the spectrum (beyond our experimental capability). Effectively, it could be manifested as CL intensity quenching. Moreover, it is possible that the increase in V_O concentration can facilitate energy transfer between the centers of luminescence as the separation between the centers decreases. When the sample is irradiated with an electron beam, the energy is transferred between the donors before it is absorbed by one center which acts as a nonradiative sink.[42] Because the polaron−vacancy association is plausible, it is likely to open up nonradiative decay paths through energy transfer between F centers. As the concentration increases beyond a critical value, energy transfer becomes efficient and leads to intensity quenching.

CONCLUSIONS

The oxygen vacancy-related CL emission from pure CeO_2 heat-treated in different atmospheres was presented here. The relative concentration of different charge states of F centers depends on the oxygen partial pressure during sintering. We found that for low oxygen pressure, F^0 centers prevail over F^+ centers in CeO_2, while for high oxygen pressure, F^+ centers are more dominant than F^0 centers. The dielectric polarizability of the CeO_2 crystal increases with decreasing oxygen partial pressure in the atmosphere of heat treatment, which confirms the continuous increase in defect concentration with decreasing oxygen partial pressure. However, the CL emission intensity does not follow this trend. Instead of a continuous increase, the CL emission reaches a maximum and starts decreasing with the increase in vacancy concentration. The polarons and associates of polarons with oxygen vacancies, such as $(V_O^{\bullet\bullet}-Ce_{Ce}')^{\bullet}$, are demonstrated as the cause of the observed CL intensity quenching at higher oxygen vacancy concentrations. The demonstrated ability of CL spectroscopy to distinguish between various charge states of oxygen vacancies is useful for defect-engineered property enhancements of CeO_2-related solid solutions.

AUTHOR INFORMATION

Corresponding Author

Matjaz Valant − *Materials Research Laboratory, University of Nova Gorica, 5270 Ajdovščina, Slovenia; Institute of Fundamental and Frontier Sciences, University of Electronic Science and Technology of China, 610054 Chengdu, China;* orcid.org/0000-0003-4842-5676; Phone: +386 53653502; Email: matjaz.valant@ung.si

Authors

Thanveer Thajudheen − *Materials Research Laboratory, University of Nova Gorica, 5270 Ajdovščina, Slovenia*

Alex G. Dixon − *Laboratory of Organic Matter Physics, University of Nova Gorica, 5270 Ajdovščina, Slovenia*

Sandra Gardonio − *Materials Research Laboratory, University of Nova Gorica, 5270 Ajdovščina, Slovenia;* orcid.org/0000-0002-5560-718X

Iztok Arčon − *Laboratory of Quantum Optics, University of Nova Gorica, SI-5000 Nova Gorica, Slovenia; Department of Low and Medium Energy Physics, J. Stefan Institute, SI-1001 Ljubljana, Slovenia*

Complete contact information is available at: https://pubs.acs.org/10.1021/acs.jpcc.0c04631

Notes

The authors declare no competing financial interest.

ACKNOWLEDGMENTS

The authors acknowledge the financial support from Ad futura, the Slovenian Research Agency (research core funding nos. P2-0412 and P1-0112), and by the project CALIPSOplus under the Grant Agreement 730872 from the EU Framework Programme for Research and Innovation HORIZON 2020. We acknowledge access to the SR facilities of ELETTRA (beamline XAFS, pr. 20185092). We would like to thank Simone Pollastri of ELETTRA for expert advice on beamline operation and for assistance during the experiment. The authors acknowledge Egon Pavlica and Luigi Giacomazzi for fruitful discussions.

REFERENCES

(1) Skorodumova, N. V.; Ahuja, R.; Simak, S. I.; Abrikosov, I. A.; Johansson, B.; Lundqvist, B. I. Electronic, Bonding, and Optical Properties of CeO2 and Ce2O3 from First Principles. *Phys. Rev. B: Condens. Matter Mater. Phys.* **2001**, *64*, 115108.

(2) Nakazawa, T.; Inoue, T.; Satoh, M.; Yamamoto, Y. Electrical Characteristics of Metal/Cerium Dioxide/Silicon Structures. *Jpn. J. Appl. Phys.* **1995**, *34*, 548−553.

(3) Pushkarev, V. V.; Kovalchuk, V. I.; d'Itri, J. L. Probing Defect Sites on the CeO $_2$ Surface with Dioxygen. *J. Phys. Chem. B* **2004**, *108*, 5341−5348.

(4) Wu, Z.; Li, M.; Howe, J.; Meyer, H. M.; Overbury, S. H. Probing Defect Sites on CeO $_2$ Nanocrystals with Well-Defined Surface Planes by Raman Spectroscopy and O $_2$ Adsorption †. *Langmuir* **2010**, *26*, 16595−16606.

(5) Spanier, J. E.; Robinson, R. D.; Zhang, F.; Chan, S.-W.; Herman, I. P. Size-Dependent Properties of CeO2−y Nanoparticles as Studied by Raman Scattering. *Phys. Rev. B: Condens. Matter Mater. Phys.* **2001**, *64*, 245407.

(6) Xu, J.; Harmer, J.; Li, G.; Chapman, T.; Collier, P.; Longworth, S.; Tsang, S. C. Size Dependent Oxygen Buffering Capacity of Ceria Nanocrystals. *Chem. Commun.* **2010**, *46*, 1887−1889.

(7) Nörenberg, H.; Briggs, G. A. D. Defect Structure of Nonstoichiometric CeO2 (111) Surfaces Studied by Scanning Tunneling Microscopy. *Phys. Rev. Lett.* **1997**, *79*, 4222−4225.

(8) Lin, Y.; Wu, Z.; Wen, J.; Poeppelmeier, K. R.; Marks, L. D. Imaging the Atomic Surface Structures of CeO2 Nanoparticles. *Nano Lett.* **2014**, *14*, 191−196.

(9) Brillson, L. J.; Ruane, W. T.; Gao, H.; Zhang, Y.; Luo, J.; von Wenckstern, H.; Grundmann, M. Spatially-Resolved Cathodoluminescence Spectroscopy of ZnO Defects. *Mater. Sci. Semicond. Process.* **2017**, *57*, 197−209.

(10) Pezzotti, G.; Leto, A. Contribution of Spatially and Spectrally Resolved Cathodoluminescence to Study Crack-Tip Phenomena in Silica Glass. *Phys. Rev. Lett.* **2009**, *103*, 175501.

(11) Boffelli, M.; Zhu, W.; Back, M.; Sponchia, G.; Francese, T.; Riello, P.; Benedetti, A.; Pezzotti, G. Oxygen Hole States in Zirconia Lattices: Quantitative Aspects of Their Cathodoluminescence Emission. *J. Phys. Chem. A* **2014**, *118*, 9828−9836.

(12) Fukatsu, K.; Leto, A.; Zhu, W.; Sugano, N.; Pezzotti, G. Kinetics and the Role of Off-Stoichiometry in the Environmentally Driven Phase Transformation of Commercially Available Zirconia Femoral Heads. *Acta Biomater.* **2012**, *8*, 1639−1647.
(13) Pezzotti, G.; Munisso, M. C.; Porporati, A. A.; Lessnau, K. On the Role of Oxygen Vacancies and Lattice Strain in the Tetragonal to Monoclinic Transformation in Alumina/Zirconia Composites and Improved Environmental Stability. *Biomaterials* **2010**, *31*, 6901−6908.
(14) Wang, D.; Park, D.; Griffith, J.; Nowick, A. Oxygen-Ion Conductivity and Defect Interactions in Yttria-Doped Ceria. *Solid State Ionics* **1981**, *2*, 95−105.
(15) Faber, J.; Geoffroy, C.; Roux, A.; Sylvestre, A.; Abélard, P. A Systematic Investigation of the Dc Electrical Conductivity of Rare-Earth Doped Ceria. *Appl. Phys. A* **1989**, *49*, 225−232.
(16) Kilner, J. Fast Oxygen Transport in Acceptor Doped Oxides. *Solid State Ionics* **2000**, *129*, 13−23.
(17) Ravel, B.; Newville, M. ATHENA, ARTEMIS, HEPHAESTUS: Data Analysis for X-Ray Absorption Spectroscopy Using IFEFFIT. *J. Synchrotron Radiat.* **2005**, *12*, 537−541.
(18) Zhang, P.; Ma, Y.; Xie, C.; Guo, Z.; He, X.; Valsami-Jones, E.; Lynch, I.; Luo, W.; Zheng, L.; Zhang, Z. Plant Species-Dependent Transformation and Translocation of Ceria Nanoparticles. *Environ. Sci.: Nano* **2019**, *6*, 60−67.
(19) Škofic, I. K.; Gomilšek, J. P.; Pihlar, B.; Kodre, A.; Bukovec, N. Structural and Electrochemical Investigations of Ce/Cu Mixed Oxide Thin Films. *Sol. Energy Mater. Sol. Cells* **2011**, *95*, 779−785.
(20) Wada, S.; Oka, K.; Watanabe, K.; Izumi, Y. Catalytic Conversion of Carbon Dioxide into Dimethyl Carbonate Using Reduced Copper-Cerium Oxide Catalysts as Low as 353 K and 1.3 MPa and the Reaction Mechanism. *Front. Chem.* **2013**, *1*, 8.
(21) Balestrieri, M.; Colis, S.; Gallart, M.; Schmerber, G.; Ziegler, M.; Gilliot, P.; Dinia, A. Photoluminescence Properties of Rare Earth (Nd, Yb, Sm, Pr)-Doped CeO2 Pellets Prepared by Solid-State Reaction. *J. Mater. Chem. C* **2015**, *3*, 7014−7021.
(22) Huang, B.; Gillen, R.; Robertson, J. Study of CeO2 and Its Native Defects by Density Functional Theory with Repulsive Potential. *J. Phys. Chem. C* **2014**, *118*, 24248−24256.
(23) Aškrabić, S.; Dohčević-Mitrović, Z. D.; Araújo, V. D.; Ionita, G.; de Lima, M. M.; Cantarero, A. F-Centre Luminescence in Nanocrystalline CeO2. *J. Phys. D: Appl. Phys.* **2013**, *46*, 495306.
(24) Tiwari, S.; Rathore, G.; Patra, N.; Yadav, A. K.; Bhattacharya, D.; Jha, S. N.; Tseng, C. M.; Liu, S. W.; Biring, S.; Sen, S. Oxygen and Cerium Defects Mediated Changes in Structural, Optical and Photoluminescence Properties of Ni Substituted CeO2. *J. Alloys Compd.* **2019**, *782*, 689−698.
(25) Smits, K.; Grigorjeva, L.; Łojkowski, W.; Fidelus, J. D. Luminescence of Oxygen Related Defects in Zirconia Nanocrystals. *Phys. Status Solidi C* **2007**, *4*, 770−773.
(26) Smits, K.; Grigorjeva, L.; Millers, D.; Sarakovskis, A.; Grabis, J.; Lojkowski, W. Intrinsic Defect Related Luminescence in ZrO2. *J. Lumin.* **2011**, *131*, 2058−2062.
(27) Yacobi, B. G.; Holt, D. B. *Cathodoluminescence Microscopy of Inorganic Solids*, 1st ed.; Springer US, 1990.
(28) Youssef, M.; Van Vliet, K. J.; Yildiz, B. Polarizing Oxygen Vacancies in Insulating Metal Oxides under a High Electric Field. *Phys. Rev. Lett.* **2017**, *119*, 126002.
(29) Adachi, G.-y.; Imanaka, N. The Binary Rare Earth Oxides. *Chem. Rev.* **1998**, *98*, 1479−1514.
(30) Chueh, W. C.; Haile, S. M. A Thermochemical Study of Ceria: Exploiting an Old Material for New Modes of Energy Conversion and CO2 Mitigation. *Philos. Trans. R. Soc., A* **2010**, *368*, 3269−3294.
(31) Henderson, M. A.; Perkins, C. L.; Engelhard, M. H.; Thevuthasan, S.; Peden, C. H. F. Redox properties of water on the oxidized and reduced surfaces of CeO2. *Surf. Sci.* **2003**, *526*, 1−18.
(32) Han, X.; Lee, J.; Yoo, H.-I. Oxygen-Vacancy-Induced Ferromagnetism in CeO2 from First Principles. *Phys. Rev. B: Condens. Matter Mater. Phys.* **2009**, *79*, 100403.
(33) Figaj, M.; Becker, K. D. An Electron Paramagnetic Resonance Study of Impurities in Ceria, CeO2. *Solid State Ionics* **2001**, *141−142*, 507−512.
(34) Costantini, J.-M.; Seo, P.; Yasuda, K.; Bhuian, A. S. I.; Ogawa, T.; Gourier, D. Cathodoluminescence of Cerium Dioxide: Combined Effects of the Electron Beam Energy and Sample Temperature. *J. Lumin.* **2020**, *226*, 117379.
(35) Zacherle, T.; Schriever, A.; De Souza, R. A.; Martin, M. Ab Initio Analysis of the Defect Structure of Ceria. *Phys. Rev. B: Condens. Matter Mater. Phys.* **2013**, *87*, 134104.
(36) Tuller, H. L.; Nowick, A. S. Small Polaron Electron Transport in Reduced Single Crystals. *J. Phys. Chem. Solids* **1977**, *38*, 859−867.
(37) Nakayama, M.; Ohshima, H.; Nogami, M.; Martin, M. A Concerted Migration Mechanism of Mixed Oxide Ion and Electron Conduction in Reduced Ceria Studied by First-Principles Density Functional Theory. *Phys. Chem. Chem. Phys.* **2012**, *14*, 6079−6084.
(38) Hughes, A. E.; Gorman, J. D.; Patterson, P. J. K.; Carter, R. Unusual Peak Shifts in the Core Levels of CeO2 Films Deposited on Si(100). *Surf. Interface Anal.* **1996**, *24*, 634−640.
(39) Bishop, S. R.; Duncan, K. L.; Wachsman, E. D. Surface and Bulk Oxygen Non-Stoichiometry and Bulk Chemical Expansion in Gadolinium-Doped Cerium Oxide. *Acta Mater.* **2009**, *57*, 3596−3605.
(40) Castleton, C. W. M.; Lee, A.; Kullgren, J. Benchmarking Density Functional Theory Functionals for Polarons in Oxides: Properties of CeO2. *J. Phys. Chem. C* **2019**, *123*, 5164−5175.
(41) Shannon, R. D. Revised Effective Ionic Radii and Systematic Studies of Interatomic Distances in Halides and Chalcogenides. *Acta Crystallogr., Sect. A: Cryst. Phys., Diffr., Theor. Gen. Crystallogr.* **1976**, *32*, 751−767.
(42) García Solé, J. *An Introduction to the Optical Spectroscopy of Inorganic Solids*. February 18, 2005, pp 1−38.

https://dx.doi.org/10.1021/acs.jpcc.0c04631
J. Phys. Chem. C 2020, 124, 19929−19936